Journal of Fluorescence (2019) 29:293–305
https://doi.org/10.1007/s10895-018-02339-z

ORIGINAL ARTICLE

NIR-Fluorescent Multidye Silica Nanoparticles with Large Stokes Shifts for Versatile Biosensing Applications

Gala Chapman[1] · Gabor Patonay[1]

Received: 23 September 2018 / Accepted: 26 December 2018 / Published online: 7 January 2019

Abstract

We have synthesized and characterized of a series of single and multidye copolymerized nanoparticles with large to very large Stokes shifts (100 to 255 nm) for versatile applications as standalone or multiplexed probes in biological matrices. Nanoparticles were prepared via the Stöber method and covalently copolymerized with various combinations of three dyes, including one novel aminocyanine dye. Covalently encapsulated dyes exhibited no significant leakage from the nanoparticle matrix after more than 200 days of storage in ethanol. Across multiple batches of nanoparticles with varying dye content, the average yields and average radii were found to be highly reproducible. Furthermore, the batch to batch variability in the relative amounts of dye incorporated was small (relative standard deviations $\leq$2.3%). Quantum yields of dye copolymerized nanoparticles were increased 50% to 1000% relative to those of their respective dye-silane conjugates, and fluorescence intensities were enhanced by approximately three orders of magnitude. Prepared nanoparticles were surface modified with polyethylene glycol and biotin and bound to streptavidin microspheres as a proof of concept. Under single wavelength excitation, microsphere-bound nanoparticles displayed readily distinguishable fluorescence signals at three different emission wavelengths, indicating their potential applications to multicolor sensing. Furthermore, nanoparticles modified with polyethylene glycol and biotin demonstrated hematoprotective qualities and reduced nonspecific binding of serum proteins, indicating their potential suitability to in vivo imaging applications.

Keywords Fluorescent silica nanoparticles · Resonance energy transfer · Large stokes shift · Near-infrared fluorescence · Multicolor assay · Biocompatible nanoparticles

Introduction

Fluorescence-based techniques play a central and crucial role in the field of bioanalytical chemistry due to their intrinsic high sensitivity and excellent spatial and temporal resolution [1–7]. Historically, these techniques have relied on the use of fluorescent dye molecules such as fluorescein, rhodamine, and cyanines as reporter tags. Near-infrared (NIR) fluorescent compounds such as heptamethine cyanine dyes are of particular utility to bioanalytical applications due to the reduced scattering and lack of interfering biomolecular autofluorescence at longer wavelengths [8–12]. However, the application of individual dye molecules has some drawbacks, including low fluorescence intensities due to limitations on the number of dye molecules that can be bound to targets, as well as the potential for undesirable environmental effects on the chemical stability and spectroscopic properties. In addition, many fluorescent dyes (particularly those with NIR fluorescence) exhibit small Stokes shifts, which hinders deconvolution of the incoming excitation light from the emission signal and predisposes the dyes to homo-quenching via resonance energy transfer between dyes of the same species [13, 14].

Fortunately, the common issue of small Stokes shifts may be addressed through introduction of different functionalities at specific locations along the chromophore in order to modulate the spectroscopic properties [15–19]. The aminocyanine dyes are a particularly notable example of this; these compounds demonstrate strongly blue-shifted absorption in accordance with the Dewar-Knott rule, resulting in a large increase in the Stokes shift, (from ~20 nm in unsubstituted cyanine dyes to >100 nm in *meso*-substituted aminocyanines)

Electronic supplementary material The online version of this article (https://doi.org/10.1007/s10895-018-02339-z) contains supplementary material, which is available to authorized users.

✉ Gala Chapman
gchapman2@student.gsu.edu

[1] Department of Chemistry, Georgia State University, P.O. Box 3965, Atlanta, GA 30302-3965, USA

[18–22]. Issues with dye stability and environmental sensitivity may also be overcome; one straightforward approach is the incorporation of fluorophores into nanoparticles [23–25]. This approach also allows for substantially higher per-label fluorescence signals owing to both increased fluorescence quantum yields and the possibility of incorporating hundreds or even thousands of dye molecules into a single fluorescent tag [4, 26]. An additional benefit of this approach is the ability to incorporate different dyes into a single label. If the incorporated dyes are capable of Förster resonance energy transfer (FRET), the effective Stokes shift of the prepared labels can be substantially increased. Furthermore, when FRET pairs are incorporated, series of nanoparticles containing different ratios and combinations of fluorescent dyes may be synthesized, resulting in a large variety of spectroscopically distinct tags from a relatively small number of starting materials. This approach produces fluorescent probes which allow for the simultaneous detection of multiple targets, thereby improving throughput capacity in multicolor sensing and imaging applications such as flow cytometry, multitarget assays, and in vivo labeling of various biological structures [27–30].

In this study, we have synthesized and characterized a series of single and multidye copolymerized silica nanoparticles possessing large to very large Stokes shifts with versatile potential applications either alone as individual fluorescence probes for biological matrices or together as a fluorescent probe series for simultaneous detection of multiple targets. Silica was chosen as the nanoparticle matrix due to the ease of both surface modification and covalent dye incorporation in order to impart maximum stability and minimize dye leaching [23, 31–33]. Aminocyanine dye GC-1-23 was designed, synthesized, and characterized, then incorporated into nanoparticles as either a lone fluorophore or as a FRET acceptor bearing a long Stokes shift. Fluorescein isothiocyanate and Texas Red were chosen as additional donor/acceptors based on their high quantum yields and spectral overlap with one another and with the aminocyanine acceptor. Fluorescent nanoparticles containing 1–3 different dyes were synthesized and characterized in terms of size, synthetic yield, quantum yield, signal enhancement, reproducibility of dye incorporation, and dye leakage after extended storage. Nanoparticles were surface-modified with polyethylene glycol and biotin and bound to magnetic streptavidin microbeads as a proof of concept for the application of these nanomaterials as single excitation multiplexing tags. Hemocompatibility and protein nonspecific binding studies were also carried out in order to assess the suitability of the nanoparticles for in vivo use.

The present work provides a framework for the facile and low-cost synthesis of fluorescent silica nanoparticles with reproducible optical properties and sizes, tunable fluorescence characteristics, excellent stability against dye leaching, and substantial enhancements to fluorescence signals relative to the individual dyes. The method is widely applicable to any dye species with appropriate reactive moieties. Furthermore, the surface-functionalized NPs demonstrate hematoprotective properties, low nonspecific protein adsorption, and amenability to bioconjugation. These properties, in combination with the large Stokes shifts and NIR fluorescence indicate a wide range of potential in vivo and in vitro biosensing applications.

Experimental

Materials and Instrumentation

Acetic acid (AcOH, glacial, ≥99%), acetonitrile (CH_3CN, CHROMASOLV® Plus, for HPLC, ≥99.9%), (3-aminopropyl)triethoxysilane (APTES, ≥ 98%), *N,N*-dimethylformamide (DMF, 99.8%), fluorescein isothiocyanate (FITC, 98%), human serum albumin (HSA, 97%), immunoglobulin G from human serum (IgG, 10 mg/mL in phosphate buffer), tetraethyl orthosilicate (TEOS, 99.999%), and 3-(triethoxysilyl)propyl isocyanate (ICPTES, 95%) were obtained from Sigma Aldrich (St. Louis, MO). Aqueous ammonia (certified ACS plus, 29.6%), methanol (MeOH, certified ACS, ≥99.8%), potassium chloride (USP), sodium chloride (certified ACS, >99.9%), sodium hydroxide (Fisher Bioreagents, ≥97.0%) sodium phosphate monobasic monohydrate (certified, ≥98%), sodium phosphate dibasic dodecahydrate (99%), and Amicon Ultra centrifugal filter units (10 kDa) were obtained from Thermo Fisher Scientific (Waltham, MA). BcMag Streptavidin Magnetic Beads (1 μm) were obtained from Bioclone Inc. (San Diego, CA). Absolute 200 proof ethanol (EtOH) was obtained from Greenfield Ethanol, Inc. (Toronto, ON). Biotin-polyethylene glycol-silane (Bio-PEG-Sil, MW 3400) and methoxypolyethylene glycol-silane (mPEG-Sil, MW 1000) were obtained from Laysan Bio (Arab, AL). Sulforhodamine 101 acid chloride (Texas Red/TR, 96.5%) was purchased from Chemodex (St. Gallen, Switzerland). Dye GC-1-23 was synthesized as detailed in the supporting information. Triply deionized water was obtained from a Barnstead Nanopure water purification system (Thermo Fisher Scientific, West Palm Beach, FL). Human red blood cells (RBCs, stabilized with CPDA-1) were obtained from Tennessee Blood Services (Memphis, TN).

All volumetric glassware (pipets used to deliver volumes greater than 1 mL and volumetric flasks) was categorized as class A. Volumes less than 1 mL were delivered using either a 10–100 μL or a 100–1000 μL adjustable volume Eppendorf pipette, and in cases where volumetric pipets or flasks were unavailable in the desired volume, volumes larger than 1 mL were delivered via a positive-displacement Eppendorf repeating pipette (Eppendorf, Hauppauge, NY.). UV-visible and fluorescence spectroscopic measurements were carried out

on Biotek Synergy H1 and Synergy H4 Microplate Readers (Biotek, Winooski, VT) and results were generated using Biotek Gen5 Software (v.2.04.11). Additional calculations, spectral processing, and spectral deconvolutions were carried out using Microsoft Excel (2016, Microsoft Corporation, Redmond, WA) and a|e - UV-Vis-IR Spectral Software (v.2.2, FluorTools, www.fluortools.com). Transmission electron microscopy (TEM) was carried out using a ZEISS Leo 906E Transmission Electron Microscope (ZEISS, Jena, Germany). Fluorescence microscopy was carried out using an Olympus BX51WI fluorescence microscope fitted with an X-Cite Series 120 Q light source and an Infinity 3S-iUR 1.4 megapixel CCD camera; microscopy images were acquired using Micro-Manager (v.1.4.22) [34, 35]. The excitation filter was a Chroma ET470/40x (470 nm/40 nm bandpass), the dichroic mirror was a Chroma T495lpxr (495 nm longpass), and the emission filters were a Chroma ET525/50 (525 nm/50 nm bandpass), an Omega EB00445B (607/45 nm bandpass), and an Omega 750DF50–0210 (750/50 nm bandpass). Microscopy images (TEM and fluorescence) were analyzed and processed using ImageJ software (v. 1.51j8) including the Align Slice and TransformJ plugins [36, 37].

Nanoparticle Synthesis

Three dye-silane conjugates were prepared for covalent incorporation into silica nanoparticles (NPs) as illustrated in Scheme 1. Fluorescein isothiocyanate (FITC) was dissolved in dry CH_3CN and combined with an excess (1.5 equivalents) of APTES; the reaction was allowed to proceed for 16 h. Texas Red (TR) was dissolved in dry DMF and combined with an excess (1.5 equivalents) of APTES; the reaction was allowed to proceed for 3 h. Aminocyanine dye GC-1-23 was dissolved in dry CH_3CN and combined with an excess (1.5 equivalents) of ICPTES; the reaction was allowed to proceed for 16 h. All reactions were conducted in closed, airtight containers at room temperature with stirring. Following conjugation reactions, dye conjugates FITC-APTES, TR-APTES, and GC-1-23-ICPTES were used "as is" and not subjected to further purification steps. Various ratios of these dye conjugates were employed in the synthesis of silica nanoparticles. Conjugates were stored at −20 °C under N_2(g) when not in use.

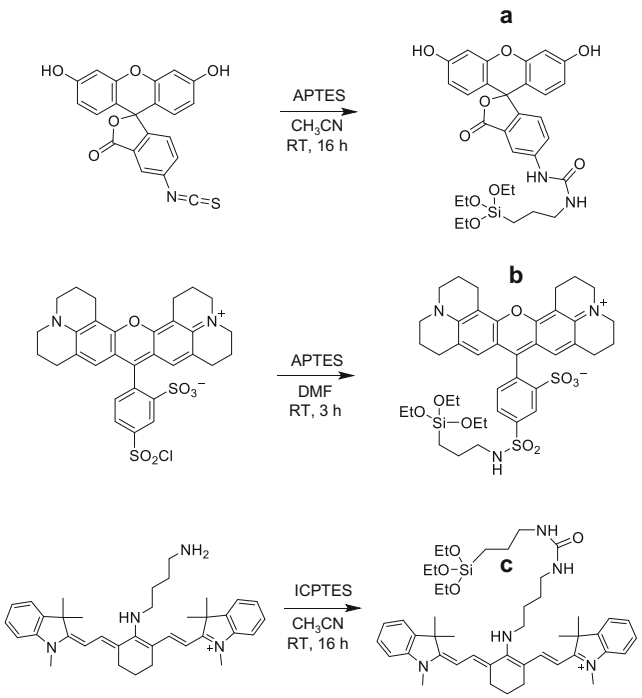

Scheme 1 Syntheses of dye-silane conjugates used in this study: **a** FITC-APTES, **b** TR-APTES, **c** GC-1-23-ICPTES

Nanoparticles (NPs) were synthesized via an adaptation of the Stöber process utilizing controlled addition of TEOS [38]. Specifically, 15.75 mL absolute EtOH, 0.780 mL water, and 0.500 mL of NH_3(aq) were added to a clean round bottomed flask equipped with a stir bar and stopper. The desired amounts of dye conjugates were added to the reaction flasks and allowed to hydrolyze for 30 min. Separately, 0.112 mL TEOS was diluted to 10.00 mL with absolute EtOH in a volumetric flask and mixed thoroughly. This solution was transferred into a syringe attached to a calibrated syringe pump, and 5.00 mL of the TEOS solution was introduced into the solution at a flow rate of 0.29 mL/h. The mixture was stirred for a total of 20 h (including TEOS addition), then the NPs were transferred to centrifuge tubes and separated from the reaction mixture by centrifugation (10,397 g for 30 min). The supernatant was removed, 15 mL EtOH was introduced into the tubes, then the centrifuge tubes were briefly placed in an ultrasonic bath to resuspend the NPs. The centrifugation/resuspension washing process was repeated three times using EtOH, and the final resuspension step was carried out into 15.00 mL EtOH delivered via a repeating pipette. Prepared NPs were stored in EtOH at 4 °C prior to further characterization.

Yields and Radii of Prepared NPs

Prepared NPs were characterized by transmission electron microscopy (TEM) in order to determine radii. Average NP sizes were used to calculate molecular weight (MW) following Eq. 1, using the average radii determined from TEM images (r, in nm) and assuming the density of the particles is identical to the published density of silica ($\rho = 2.2$ g/cm^3) [39, 40]. In this equation, N_A is Avogadro's number and 10^{-21} is a conversion factor from cm^3 to nm^3.

$$\text{MW NPs (g/mol)} = \frac{4}{3}\pi r^3 \rho N_A \times 10^{-21} \quad (1)$$

Gravimetric NP yields were determined as follows: exactly half of each NP solution (in EtOH) was transferred

to a tared vial and dried using a controlled stream of dry N_2, then further dried in an oven at 110 °C. Oven-dried NP samples were brought to room temperature in a desiccator prior to weighing. Concentrations could then be determined for the remaining solution based on the known solution volume, calculated molecular weight, and yield.

Surface Modification of NPs for Biosensing Applications

The prepared multifluorescent NPs appear to be excellent candidates for in vitro or in vivo biosensing applications due to their NIR fluorescence and long Stokes shifts. However, NP surfaces must be passivated to reduce issues with flocculation, toxicity, and nonspecific binding to biomolecules. Furthermore, appropriate functionalities must be introduced in order to promote bioconjugation for in vitro assay development. Bare silica nanoparticles were modified with polyethylene glycol derivatives for the purposes of both surface passivation and the introduction of biotin moieties for bioconjugation. Cleaned NPs in EtOH (~0.9 mg/mL) were aliquoted into centrifuge tubes fitted with stir bars. Separately, solutions containing 50 mg/mL Bio-PEG-Sil and 70 mg/mL mPEG-Sil were prepared in 1 mM AcOH(aq) and allowed to prehydrolyze for 10 min. Following the prehydrolysis time, appropriate volumes of Bio-PEG-Sil and mPEG-Sil solutions were introduced. To produce biotin- and PEG-functionalized particles (BPNPs) suitable for avidin binding, theoretical surface coverage densities of 4.0 μmol/m^2 Bio-PEG-Sil and 36 μmol/m^2 mPEG-Sil were introduced. For plain surface-passivated PEGylated particles lacking the biotin functionality (PNPs), a theoretical surface coverage density of 40 μmol/m^2 mPEG-Sil was introduced. Surface coverage densities were calculated using the specific surface area (SSA), as given in Eq. 2. In this equation, d is the NP diameter (in nm) and ρ is the density of silica (2.2 g/cm^3) [40–42].

$$\mathrm{SSA}\left(\mathrm{m}^2/\mathrm{g}\right) = \frac{6000}{\mathrm{d}\rho} \tag{2}$$

The reactions were allowed to proceed at room temperature for 2 h, then the surface modified nanoparticles (BPNPs and PNPs) were centrifuge washed three times with a 50% EtOH in water mixture to remove any excess unreacted silane, with resuspension sonication steps carried out in an ice bath to reduce the likelihood of PEG sonolysis [43]. The functionalized BPNPs were stored in 50% EtOH/water mixtures at 4 °C prior to characterization and application.

Results and Discussion

Dye Pair Design

Heptamethine aminocyanine dye GC-1-23 was synthesized as detailed in the supplementary information (Section S.1). GC-1-23 was designed as a NIR-fluorescent dye with both a *meso* secondary amino moiety imparting a long Stokes shift and a secondary reactive terminal primary amine for covalent incorporation into silica NPs via reaction with ICPTES (Scheme 1). Spectroscopic characteristics (molar absorptivity, quantum yield, Stokes shift) of the native dye were assessed in MeOH (Section S.2). The experimentally determined molar absorptivity (ε) of this dye was 2.7(±0.17)×10^4 M^{-1} cm^{-1} ($n = 5$), the quantum yield (ϕ) determined in triplicate relative to the standard indocyanine green [44] was 0.21(±0.099). Absorption and emission spectra for the dye are provided in Fig. S.1, highlighting a rather large Stokes shift of 118 nm. The experimentally determined quantum yield, molar absorptivity, and Stokes shift all fall within previously reported ranges for aminocyanines [20–22]. The basis for the large Stokes shift observed in cyanine dyes with *meso* amino substitution may be explained in terms of the Dewar-Knott rule [18–20]. In conjugated systems, amino groups demonstrate a net electron-donating character due to strong resonance effects; this character is only slightly attenuated by weaker electron-withdrawing inductive effects. Substitution with electron-donating amino moieties at the *meso* carbon results in a stabilizing effect on the highest occupied molecular orbital (HOMO) without comparable concomitant effect on the lowest unoccupied molecular orbital (LUMO), thereby increasing the energy gap between these orbitals and blue-shifting the absorption spectrum. The increased Stokes shift occurs as a smaller shift is observed in the fluorescence spectrum, due in part to the energy cost associated with the excited state intramolecular charge transfer that occurs in these compounds [20, 45].

Xanthene dyes FITC and TR were covalently incorporated into NPs via their respective conjugates with APTES (Scheme 1). The neutral lactone tautomer of FITC has been illustrated in this scheme due to the predominance of this form in aprotic solvents [46]. Normalized fluorescence spectra and absorption spectra (corrected for scattering) for each of the dye conjugates covalently incorporated into silica NPs are provided in Fig. 1. The absorption spectra for both the primary and secondary acceptor dyes (TR and GC-1-23) exhibit significant overlap with the fluorescence spectrum of the primary donor (FITC). This observation indicates that FITC is likely to be a suitable FRET donor for both TR and GC-1-23, as a major requirement for successful energy transfer is that the emission energy of the donor matches the excitation energy requirements of the acceptor. More specifically, the extent of energy transfer is dependent upon the area of overlap between the donor emission and acceptor excitation spectra [2, 47].

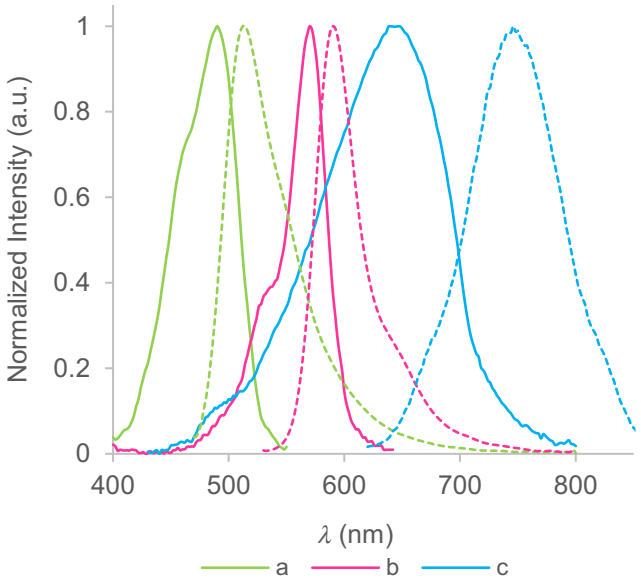

Fig. 1 Normalized absorption (solid) and fluorescence (dashed) spectra from single dye copolymerized NPs: **a** FITC-NPs (1:0:0 dye ratio), **b** TR-NPs (0:1:0 dye ratio), **c** GC-1-23-NPs (0:0:2 dye ratio)

Copolymerization of silica nanoparticles with combinations of these dye molecules at appropriate concentrations should therefore be capable of increasing the effective Stokes shift of the nanoparticles via FRET interactions between the constituent dyes.

Optimization of Dye Ratios and Fluorescence Characterization of Single and Multidye NPs

Dye-silane concentrations were optimized for fluorescence intensities in preliminary studies (Section S.3); the optimal molar dye ratio (FITC:TR:GC-1-23) was found to be 1:1:2 (in which one equivalent represents 0.025 mol% of dye-silane conjugate added relative to TEOS). Fluorescence intensities decreased for NPs incorporating higher dye-silane concentrations than this, presumably as a result of homo-FRET or possibly self-quenching interactions. A "family" of fluorescent NPs was then synthesized for the primary focus of this study. This group comprised all possible combinations of single and multiple dyes based on the optimized "1:1:2" molar ratio; ratios of FITC:TR:GC-1-23 in the synthesized NPs were as follows: 1:0:0, 0:1:0, 0:0:2, 1:1:0, 1:0:2, 0:1:2, and 1:1:2. Selected NPs from this family were chosen for further characterization. Photographs of these NPs in EtOH under ambient light and UV light are depicted in Fig. 2. Under short-wavelength excitation (365 nm), the brightest visible fluorescence is observed for the 1:1:0 NPs, although bright fluorescence is also readily observed for the 1:0:0 and 0:1:0 NPs. Fluorescence spectra acquired for these three NP samples under a longer, more suitable excitation wavelength (λ_{EXC}) for donor FITC (450 nm) are provided in Fig. 3. A comparison of the relative intensities of the fluorescence spectra of the 1:0:0,

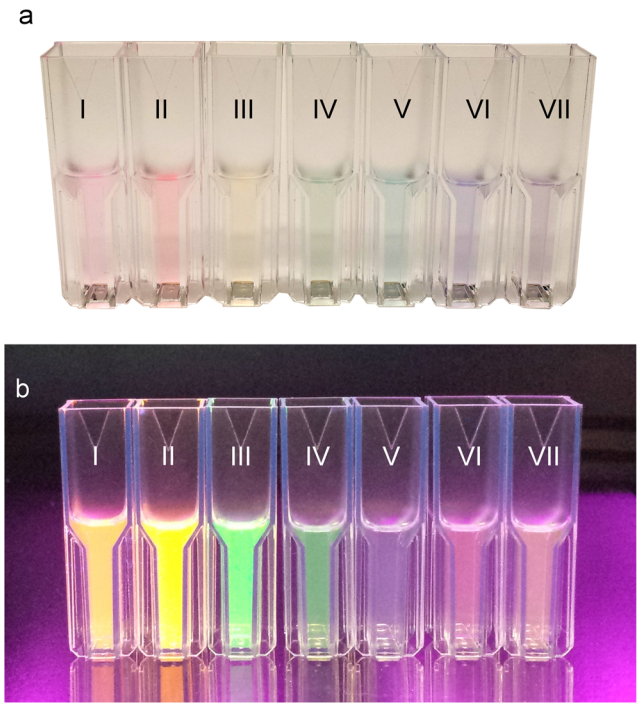

Fig. 2 Comparison of single- and multidye-copolymerized NP samples under (**a**) ambient lighting and (**b**) ultraviolet lighting (365 nm). Dye molar ratios (FITC:TR:GC-1-23) for these samples were: (I) 0:1:0, (II) 1:1:0, (III) 1:0:0, (IV) 1:0:2, (V) 0:0:2, (VI) 0:1:2, and (VII) 1:1:2

0:1:0 and 1:1:0 NPs indicate an unexpectedly intense fluorescence enhancement for the 1:1:0 NPs upon excitation at 450 nm, with a net fluorescence intensity (I_F) at the maximum emission wavelength 2.3 times that of NPs copolymerized with an equivalent amount of the donor alone (1:0:0) and more than 20 times that of the acceptor alone. This may be partially

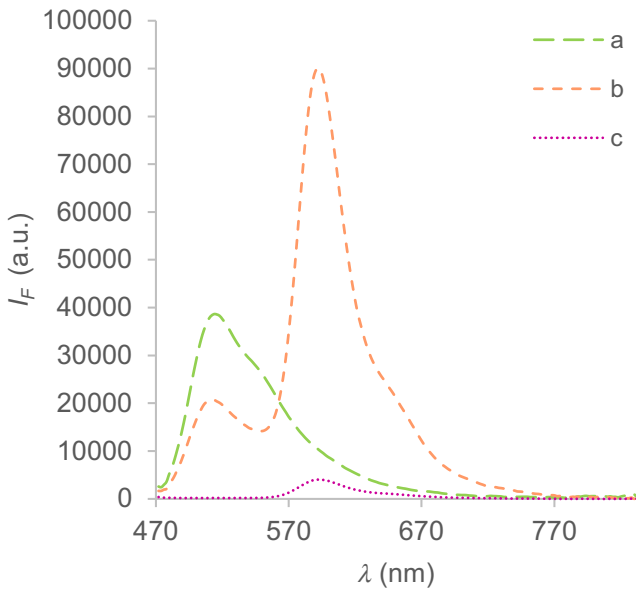

Fig. 3 Fluorescence spectra for NPs copolymerized with FITC:TR:GC-1-23 in the ratios (**a**) 1:0:0, (**b**) 1:1:0, (**c**) 0:1:0 obtained using an excitation wavelength (λ_{EXC}) of 450 nm

attributable to the very high quantum yield of the acceptor and the apparent high energy transfer efficiency between the donor and acceptor. These ultrabright particles are potentially very useful for high-sensitivity imaging applications and feature a large Stokes shift of 100 nm. Stokes shifts were further increased to 255 nm through the addition of aminocyanine dye GC-1-23 at the expected trade-off of lower overall intensities than those exhibited by the 1:0:0 NPs and 1:1:0 NPs due to efficient energy transfer, the lower quantum yield of the aminocyanine acceptor, and the energy loss corresponding to the large Stokes shift of the acceptor. Fluorescence spectra for the 1:1:2 and 1:0:2 NPs (λ_{EXC} = 450 nm) containing this aminocyanine dye are provided in Fig. 4. The NIR fluorescence and very large Stokes shifts exhibited by these materials are good indicators of suitability for applications as fluorescent tags in complex biological matrices. Also included in this figure are spectra for the 0:1:2 and 0:0:2 NPs under the same λ_{EXC} for comparison; observed fluorescence intensities for these materials were significantly lower given the absence of the donor (FITC).

NP Yields and Sizes

A summary of the experimentally determined NP yields and average radii (r, with included standard deviations, n = 30) for six separate samples of NPs containing different dye combinations is provided in Table 1. Also included in this table are averages ($\overline{x}$), standard deviations (s), and percent relative standard deviations (%RSD) of all the determined yields and radii across the six separate batches. A representative TEM image of prepared NPs is provided in Fig. 5.

Table 1 Synthesis yields and TEM radii for NPs with different dye combinations

NP Sample	Yield (mg)	r (nm)
1:0:0	14.05	38 ± 6.2
0:1:0	13.40	41 ± 6.8
0:0:2	13.62	35 ± 5.5
1:1:0	12.45	38 ± 3.9
1:0:2	14.00	39 ± 5.6
1:1:2	12.83	36 ± 5.8
$\overline{x}$ (all)	13.4	38
s (all)	0.59	2.0
%RSD (all)	4.4%	5.3%

For NPs synthesized using the Stöber process, it has been shown that polydispersity increases with decreasing NP radius [48]; the prepared particles were on the smaller end of the Stöber size range and the measured radii displayed within-batch standard deviations ranging from 3.9–6.8 nm (10–17% RSD). The average radius among the six separate batches was 38 nm, and despite the different combinations and total amounts of dye-silane conjugates added to these different NP syntheses the batch-to-batch variation in average radius was small (±2 nm; 5.3% RSD) and not statistically significant. Average NP yields were also reproducible with a batch-to-batch RSD of 4.4%. The apparent reproducibility of both the average radius (regardless of dye content and combination) and the average yield is particularly useful in downstream calculations requiring NP concentrations and surface areas, such as calculations for the surface coating and streptavidin-binding steps.

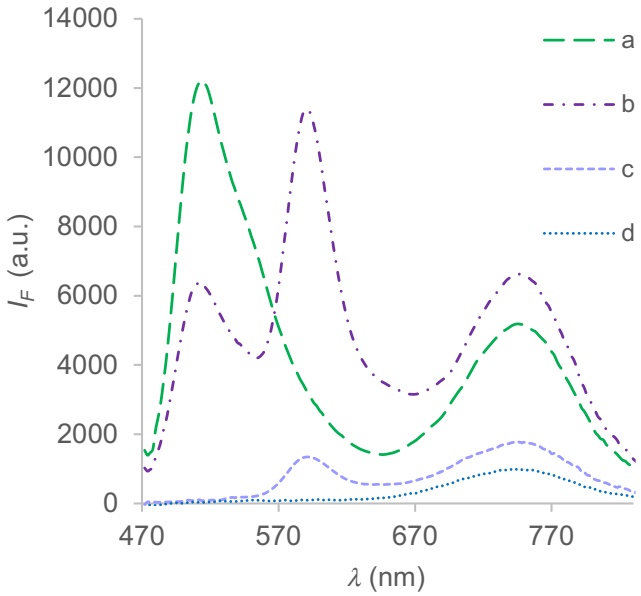

Fig. 4 Fluorescence spectra for NPs copolymerized with FITC:TR:GC-1-23 in the ratios (**a**) 1:0:2, (**b**) 1:1:2, (**c**) 0:1:2, (**d**) 0:0:2 obtained using an excitation wavelength (λ_{EXC}) of 450 nm

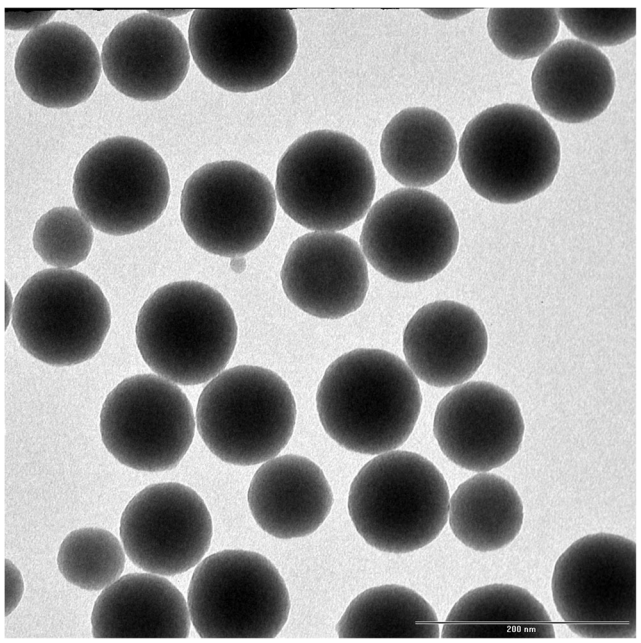

Fig. 5 Representative TEM image of prepared NPs (scale bar: 200 nm)

Reproducibility of Dye Incorporation in NPs

Reproducibility of dye incorporation was determined using relative peak intensities determined from three separate syntheses of 1:1:2 NPs as detailed in Section S.4 of the supporting information; results are provided in Table S.2. The incorporation rate appears to be very repeatable across multiple syntheses from a given dye-silane stock solution; the maximum observed batch-to-batch relative standard deviation for the calculated fluorescence ratios was 2.3%. This observed high batch-to-batch reproducibility of dye incorporation ratios, alongside the previously mentioned reproducibility of average radius and yield are promising indicators that these NPs may serve as reliable and consistent fluorescent labels regardless of the synthesis batch and choice of incorporated fluorophores. Additionally, the reproducibility of fluorescence ratios suggests that moderate adjustments to individual dye concentrations could produce additional fluorescent tags with readily distinguishable intensities at monitored wavelengths, further expanding the combinatorial possibilities for multicolor imaging.

Dye Leaching

Dye leaching was assessed in EtOH solutions of NPs stored for 205 days by separating the supernatant from a batch of 1:1:2 NPs and assessing the fluorescence intensity as a percentage of that observed for the intact NP solution, as detailed in Section S.5 of the supporting information; results are provided in Table S.3. The highest leaching percentage was observed for FITC; after 205 days, the percent relative fluorescence intensity of the supernatant was 1.5% of the total fluorescence. This good resistance to dye leaching both highlights the importance of covalent dye incorporation and indicates the long-term longevity of the prepared NPs.

Quantum Yield

Quantum yields of dye-silane conjugates and single dye copolymerized nanoparticles were calculated as detailed in the supporting information (Section S.6). Quantum yields for FITC-APTES and FITC-NPs (1:0:0) were determined in EtOH relative to fluorescein (F) in 0.1 M NaOH, quantum yields for TR-APTES and TR-NPs (0:1:0) were determined in EtOH relative to rhodamine 6G (R6G) in EtOH, and quantum yields for GC-1-23-ICPTES and GC-1-23-NPs (0:0:2) were determined relative to the previously characterized value for GC-1-23 in MeOH. The standards were chosen for similarity of spectroscopic characteristics to those of the dyes and NPs in order to circumvent potential wavelength-dependent variations in detector response. Average quantum yields (ϕ, with included standard deviations, $n = 3$) for dye conjugates and their respective dye copolymerized NPs are provided in Table 2. Also provided in this table are the standards used (S) and the published quantum yields of the standards (ϕ_S).

Experimentally determined quantum yields were reproducible; relative standard deviations ranging from 2.0–4.8% were observed. Quantum yields of dyes in NPs increased substantially relative to those determined for the dye-silane conjugates in EtOH (50% to 1000%). Substantial enhancements in fluorophore quantum yield upon encapsulation into NPs have been previously documented in the literature and attributed to decreases in the nonradiative rate for dyes restricted within the NP polymeric matrix [26, 49–51]. The calculated 100% quantum yield of Texas Red NPs (0:1:0) likely contributes to the unexpectedly large fluorescence intensity enhancement observed in the acceptor emission for the 1:1:0 NPs. Interestingly, the calculated quantum yield of the TR-APTES conjugate in EtOH is substantially lower than that published for Texas Red in the same solvent ($\phi = 0.93$) [52]. This is likely a substitution effect consequential to the direct conjugation of the reactive sulfonyl chloride group with the chromophore; in this case, conversion of this group to a sulfonamide via reaction with APTES (Scheme 1) modulates the fluorescence yield through an increase in the electron-donating properties [53]. No such strong effect is observed for the GC-1-23-ICPTES conjugate and only a minor change in quantum yield is measured upon reaction of GC-1-23 with ICPTES; this observation endorses the preferential reaction between isocyanate and the terminal primary amine due to the lack of conjugation between this amino group and the dye chromophore (Scheme 1).

Both the substantially larger relative increase in FITC-APTES quantum yield (1000%) upon incorporation into NPs relative to those increases observed for the other dye-silanes and the low observed quantum yield of FITC-APTES conjugate in EtOH may be attributable to the difference in protonation state of FITC-APTES in ethanol relative

Table 2 Quantum yields calculated for dye-silane conjugates and dye copolymerized NPs (n = 3)

Standard (S)	ϕ_S	λ_{EXC} (nm)	Sample	ϕ
F	0.925[a]	450	FITC-APTES	0.044 ± 0.0020
			1:0:0 NPs	0.49 ± 0.014
R6G	0.95[a]	510	TR-APTES	0.61 ± 0.020
			0:1:0 NPs	1.0 ± 0.021
GC-1-23	0.21[b]	650	GC-1-23 -ICPTES	0.25 ± 0.012
			0:0:2 NPs	0.39 ± 0.018

[a] Magde D, Wong R, Seybold PG (2002) Fluorescence Quantum Yields and Their Relation to Lifetimes of Rhodamine 6G and Fluorescein in Nine Solvents: Improved Absolute Standards for Quantum Yields. Photochem Photobiol 75(4): 327–334. https://doi.org/10.1562/0031-8655(2002)0750327FQYATR2.0.CO2

[b] Standardized relative to indocyanine green (supporting information Section S.2)

to that upon incorporation into silica nanoparticles. This supposition is supported by the normalized spectra included in Fig. 6; the broad peaks exhibited by FITC-APTES in EtOH implies the majority of fluorescein is in its nonfluorescent neutral form, whereas the corresponding sets of spectra for both FITC NPs (1:0:0) and fluorescein standard in base solution (0.1 M NaOH) indicate relatively larger proportions of the fluorescent deprotonated forms of fluorescein [54]. The reduction in quantum yield and spectroscopic differences observed for both FITC-APTES and FITC 1:0:0 NPs relative to those of standard fluorescein in basic solution are likely attributable to a combination of differences in solvents and local environments resulting in differing protonation status as well as differences in dye substitution resulting in changes to the extent of photoinduced electron transfer. The isothiocyanate group present on FITC is conjugated with the xanthene chromophore in a manner analogous to the sulfonyl chloride group present on Texas red (Scheme 1); substitution at this moiety has previously been shown to result in changes to both quantum yield and spectra [55, 56]. Nonetheless, the experimentally determined quantum yield for the FITC NPs (1:0:0) was in close agreement with the value published previously by Hu et al. for FITC NPs prepared in their lab ($\phi = 0.52$) [57].

Fluorescence Enhancement of Dye Copolymerized NPs

The fluorescence enhancement of the constituent dyes upon encapsulation into NPs was determined as the ratio of average limits of detection for the individual dye-silane conjugates (LOD_{DYE}) with those of their respective dye-containing NPs (LOD_{NP}). Experimental details are provided in the supporting information (Section S.7). The calculated LOD values (as averages ± standard deviations) and ratios of average LOD values are presented in Table 3. Curves constructed for the calculation of LOD values all demonstrated coefficients of determination (R^2) greater than 0.99, indicating acceptable linearity. The calculated detection limit ratios reveal that the sensitivity is improved by approximately three orders of magnitude for the fluorescent NPs relative to their constituent dye-silane conjugates; this substantial enhancement in sensitivity may be attributed to both the large numbers of dye molecules encapsulated per NP and the substantial increases in quantum yield exhibited by the particle-bound dyes relative to their respective dye-silane conjugates.

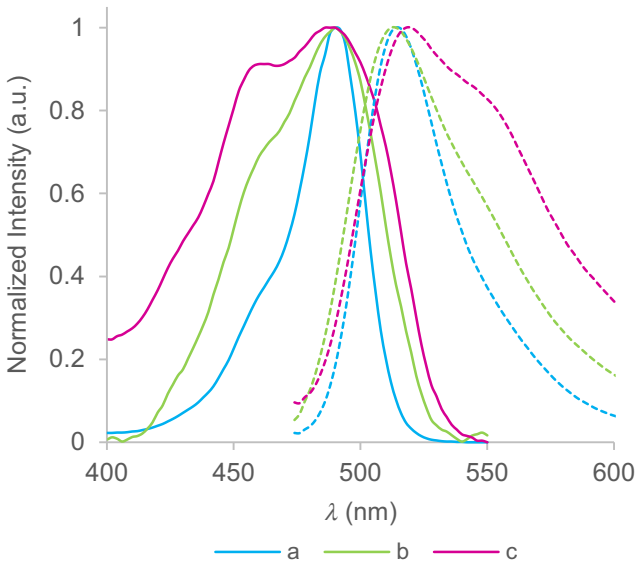

Fig. 6 Normalized absorption (solid) and emission (dashed) spectra for fluorescein species in different environments: **a** fluorescein standard in base solution, **b** FITC-APTES copolymerized NPs in EtOH (1:0:0), and **c** FITC-APTES conjugate in EtOH

Demonstration of In Vitro Applicability to Multitarget Imaging

One major advantage of silica as a matrix for fluorescent dyes is its amenability to surface modification. Polyethylene glycol (PEG) is particularly useful for applications in biological matrices as it is effective in both reducing NP flocculation and shielding NP surfaces from unwanted nonspecific surface interactions with proteins [4, 58]. For bioconjugation purposes, the streptavidin-biotin system is of tremendous utility due to the binding specificity of streptavidin and the rapid formation, stability, and near-covalent strength of the bond ($K_d = 4 \times 10^{-14}$) between this protein and its target biotin [59]. Accordingly, the series of four NPs containing donor FITC (1:0:0, 1:1:0, 1:0:2, and 1:1:2 NPs) were surface functionalized with a combination of silane derivatives of methoxy-PEG (mPEG-Sil) and biotin-PEG (Bio-PEG-Sil) to produce biotin-PEG-nanoparticles (BPNPs). These NPs were then conjugated to magnetic streptavidin microspheres and imaged with fluorescence microscopy as a proof of concept for these probes to in vitro multitarget assays; experimental details are provided in the supporting information (Section S.8). Fluorescence was measured using single wavelength excitation (470 nm) and emissions were imaged using three separate filters (with nominal wavelengths of 525 nm, 607 nm, and 750 nm). Fluorescence images obtained at each emission wavelength and corresponding brightfield overlays of the BPNP-microsphere conjugate samples are provided in Fig. 7. The fluorescence colors chosen for the respective emission channels in this figure are representative of the nominal wavelengths of the emission filters used in this study.

The streptavidin microbeads demonstrated a tendency towards aggregation following slide spotting and drying regardless of whether they were functionalized with NPs. Blank particles exhibited no apparent intrinsic fluorescence at any of the monitored wavelengths. Upon single-wavelength excitation at 470 nm, the fluorescence images for tags with differing dye contents demonstrate markedly different filter-specific

Table 3 Calculated average LOD values for NPs and dye-silane conjugates ($n = 3$) and their ratios

NP Sample	Dye-Silane	LOD_{NP} (M)	LOD_{DYE} (M)	LOD_{DYE}/LOD_{NP}
1:0:0	FITC-APTES	1.38(+0.025)E-13	8.2(±0.12)E-10	5.9E+03
0:1:0	TR-APTES	6.5(±0.27)E-14	6.3(±0.17)E-11	9.8E+02
0:0:2	GC-1-23-ICPTES	3.2(±0.12)E-12	6.0(±0.25)E-09	1.9E+03

fluorescence from each dye in its corresponding channel, allowing ready differentiation even by simple visual inspection of the individual fluorescence channels. This characteristic greatly facilitates the distinction of targets in multicolor imaging applications. In future studies, these biotinylated NPs could readily be further functionalized with avidin and linked to biotinylated antibodies or oligonucleotides for applications in a variety of multicolor assays.

Assessment of Biocompatibility for In Vivo Applications

Fluorescent silica NPs are attractive probes for in vivo applications owing to their high fluorescence intensities and their reduced sensitivity to environmental conditions, and NIR-fluorescent NPs are particularly attractive candidates due to the lack of interfering fluorescence from biomolecules in this wavelength range. However, the surfaces of bare silica NPs tend to adsorb proteins in vivo; formation of these protein coronas alters the surface characteristics as well as the biological outcomes of interactions between NPs and living systems [60]. Additionally, bare silica NPs demonstrate significant hematotoxicity, which further limits their suitability to applications in biological systems [61]. Accordingly, NPs prepared with varying surface coating regimes were assessed for both hemolytic effects and extent of protein adsorption using slight modifications to methods described previously [61, 62]; details of the experimental approaches are provided in the supporting information (Sections S.9 and S.10). The representative NP samples for both studies all had a 1:1:2 dye ratio and differing surface modifications: bare 1:1:2 NPs, mPEG-only 1:1:2 PNPs, and 1:1:2 BPNPs with dual Bio-PEG-Sil and mPEG-Sil surface functionalization. Hemolysis experiments were conducted using human red blood cells (RBCs) and nonspecific binding was assessed using human serum albumin (HSA) and human immunoglobulin G (IgG) as model proteins. HSA was selected as it is a major constituent of blood as well as a key transport protein, and IgG was chosen due to the fact that it is the most common serum antibody and a major actor in immune response.

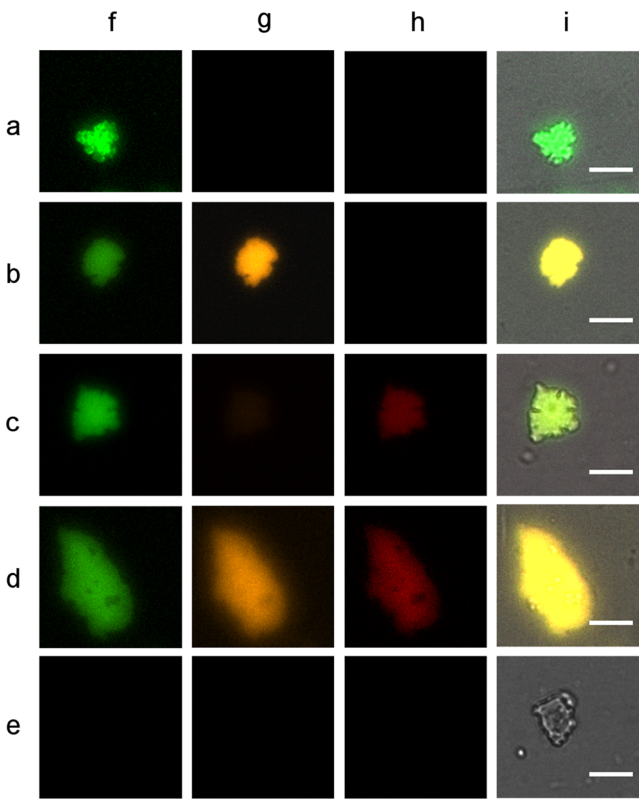

Fig. 7 Fluorescence microscopy images of streptavidin microbeads conjugated with BPNPs with FITC:TR:GC-1-23 dye ratios of (**a**) 1:0:0, (**b**) 1:1:0, (**c**) 1:0:2, (**d**) 1:1:2; corresponding images of blank streptavidin microbeads are provided in (**e**). For all samples, the excitation filter nominal wavelength was 470 nm and the emission filter nominal wavelengths were (**f**) 525 nm, (**g**) 607 nm, (**h**) 750 nm. Combined emission spectra overlaid on brightfield images are provided in column (**i**); scale bar: 10 μm

Bare silica NPs demonstrated substantial hematotoxicity (42% hemolysis) at a concentration of 1 mg/mL. However, following PEGylation of the NP surface, a dramatic reduction in hemolytic effects was observed; hemolysis percentages observed for equal concentrations of PNPs and BPNPs were found to be −0.3% and − 0.4%, respectively, as a result of hemoglobin absorption values below those of the negative control. The hematoprotective effects observed following PEGylation of NPs indicate effective surface passivation for these materials, shielding RBC membranes from destabilizing interactions with the highly charged surface silanol groups [63]. Efficient surface passivation may also explain the decrease in nonspecific adsorption of both HSA and IgG by the PEGylated particles relative to bare NPs, as illustrated in Fig. 8. At nanoparticle concentrations of 2.5 mg/mL, the weight percent adsoption efficiency for IgG decreased from 4.8% for bare NPs to 1.0% for PNPs and 1.3% for BPNPs. Under the same conditions, weight percent adsorption efficiency for HSA decreased from 3.3% for bare NPs to 1.8% for PNPs and 2.4% for BPNPs. Protein-surface interactions

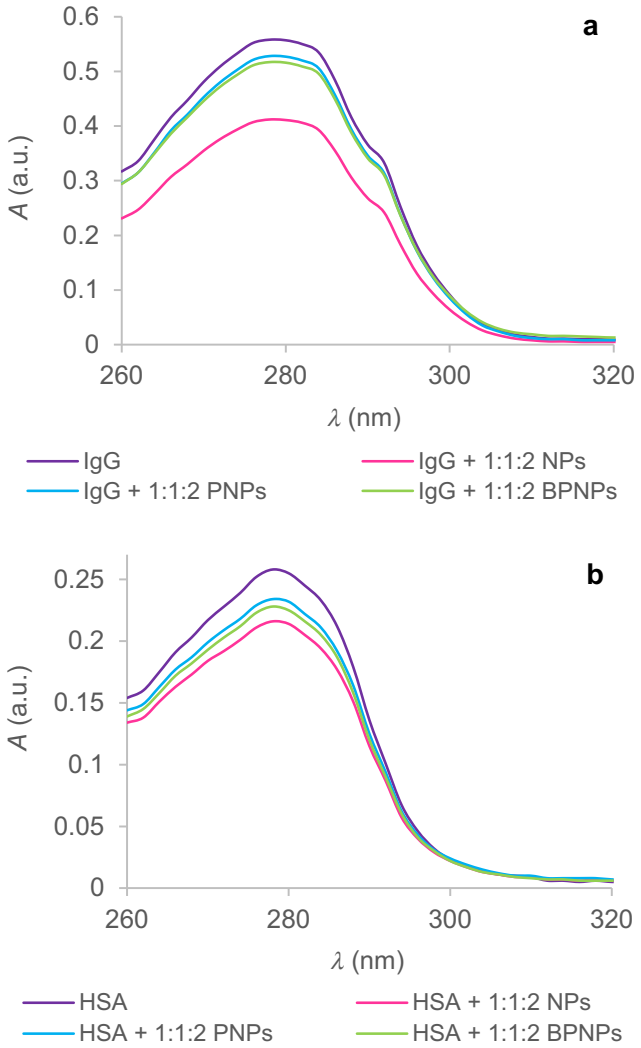

Fig. 8 Absorption spectra of (**a**) IgG and (**b**) HSA solutions following incubation with bare 1:1:2 NPs, PEGylated 1:1:2 PNPs, and 1:1:2 BPNPs functionalized with both PEG and biotin

occur as a result of a combination of electrostatic, Van der Waals, and steric interactions; introduction of PEG to the NP surface reduces both the strength and extent of these interactions through a combination of steric repulsion and charge shielding [61]. It is notable that, when comparing PEGylated PNPs and BPNPs, the BPNPs exhibited a somewhat higher percentage of protein adsorption than the PNPs for both proteins studied; the cause of this is not entirely clear but may be related to either the increased PEG chain length in Bio-PEG-Sil (MW 3400 vs MW 1000 for mPEG-Sil) or protein interactions with the terminal biotin moieties. This observation warrants further study. Nonetheless, the major improvement in hemocompatibility and the significant reduction in protein adsorption for the PEGylated PNPs and BPNPs indicates that NPs with these surface coating regimes are promising candidates for in vivo bioimaging applications. Nanoparticles containing either a combination of TR and GC-1-23 (0:1:2 NPs) or GC-1-23 only (0:0:2 NPs) should be well-suited to fluorescence imaging of sensitive biological tissues due to their lower energy excitation ranges. Moreover, for the clear, low-background imaging of whole organisms, 0:0:2 NPs should be ideal probes due to the high quantum yield and large Stokes shift of this dye, the transparency of biological tissues at its excitation wavelength, and the negligible autofluorescence background at its emission. Furthermore, as previously demonstrated using streptavidin microspheres, the biotinylated BPNPs readily bind to avidin species, allowing further functionalization of NPs with biotinylated antibodies or aptamers for selective targeting of cell types and tissues. These applications will be the focus of future work.

Conclusions

Aminocyanine dye GC-1-23 was synthesized and characterized; this dye exhibited a large Stokes shift and high quantum yield. A series of versatile, multifluorescent NPs with large Stokes shifts based on copolymerization with FITC, TR, and GC-1-23 was synthesized, characterized, and modified for bioconjugation. The prepared NPs exhibit minimal dye leaching even after more than 200 days of continuous storage in EtOH, and ratios of fluorescence intensities are reproducible from batch to batch. Regardless of dye content and the dyes used, both the average diameter and yield of the prepared NPs are reproducible. The independence of size on dye content and the low batch-to-batch variability in yield between individual syntheses eases calculations reliant on NP size and concentration, reduces the need for extensive characterizations of individual NP syntheses prior to application, and reduces the likelihood of size-dependent variations in interactions with biological targets [64]. The prepared NPs exhibited high quantum yields and substantial increases in fluorescence intensities relative to their constituent dye-silane conjugates. Following PEGylation and surface modification with biotin, proof of concept for these probes to in vitro multicolor assays was demonstrated through binding to magnetic streptavidin beads and fluorescence microscopy imaging. Furthermore, the reduced protein adsorption and hematoprotective properties demonstrated by PEGylated NPs indicate their promising potential for in vivo imaging.

The present study details an approach through which a variety of biocompatible NPs with readily distinguishable fluorescence signals and large Stokes shifts can be prepared using common laboratory equipment and a small number of relatively inexpensive starting materials. To the best of our knowledge, NPs containing FITC and GC-1-23 feature the largest Stokes shifts of any multidye NP tags produced to date. Of the NPs synthesized, the four NP combinations with significant absorption at 450 nm (1:0:0, 1:1:0, 1:1:2, 1:0:2) could be applied as fluorescent barcodes for a single excitation multitarget assay, with individual fluorescence signals

deconvoluted on the basis of fluorescence signals at characteristic wavelengths for each dye. The combinatorial possibilities could be expanded further by varying the relative dye ratios or incorporating additional dye species. Moreover, some of the individual synthesized NPs demonstrate particular strengths. For example, the brightly fluorescent FITC-TR 1:1:0 NPs in should make excellent labels for applications requiring high sensitivity, and particles encapsulating GC-1-23 (0:0:2 NPs) should lend themselves nicely to in vivo applications due to their longer wavelength absorption in the biological transparency window, NIR fluorescence, high quantum yield, and large Stokes shifts.

Acknowledgements We would like to thank Dr. Robert Simmons for supplying TEM spectra, Sharon Flores and Gyliann Peña for providing hematology samples, Maksim Kvetny and Dr. Gangli Wang for assisting with fluorescence microscopy instrumentation and image collection, Dr. Rudolph Johnson for providing spectrofluorometer access, and Stephanie Negrete and Dr. Jonas Perez for facilitating the usage of this instrument. This research was supported in part with a Georgia State University Dissertation Grant.

Compliance with Ethical Standards

Conflict of Interest The authors declare that they have no conflict of interest.

Publisher's Note Springer Nature remains neutral with regard to jurisdictional claims in published maps and institutional affiliations.

References

1. Fluorescence Microscopy and Fluorescent Probes (1998), vol 2. Plenum Press, New York & London
2. Lakowicz JR (2006) Principles of fluorescence spectroscopy, 3rd edn. Springer Science+Business Media, LLC, New York
3. Doré K, Leclerc M, Boudreau D (2006) Investigation of a fluorescence signal amplification mechanism used for the direct molecular detection of nucleic acids. J Fluoresc 16:259–265. https://doi.org/10.1007/s10895-006-0098-4
4. Estévez MC, O'Donoghue MB, Chen X, Tan W (2009) Highly fluorescent dye-doped silica nanoparticles increase flow cytometry sensitivity for cancer cell monitoring. Nano Res 2(6):448–461. https://doi.org/10.1007/s12274-009-9041-8
5. Weissleder R, Tung C-H, Mahmood U, Bogdanov A Jr (1999) In vivo imaging of tumors with protease-activated near-infrared fluorescent probes. Nat Biotechnol 17:375–378. https://doi.org/10.1038/7933
6. Shalon D, Smith SJ, Brown PO (1996) A DNA microarray system for analyzing complex DNA samples using two-color fluorescent probe hybridization. Genome Res 6(7):639–645. https://doi.org/10.1101/gr.6.7.639
7. Lanz E, Gregor M, Slavík J, Kotyk A (1997) Use of FITC as a fluorescent probe for intracellular pH measurement. J Fluoresc 7(4):317–319. https://doi.org/10.1023/A:1022586127784
8. Dawson PL, Acton JC (2018) 22 - impact of proteins on food color. In: Yada RY (ed) Proteins in food processing, Second edn. Woodhead Publishing, Cambridge, pp 599–638. https://doi.org/10.1016/B978-0-08-100722-8.00023-1
9. Zipfel WR, Williams RM, Christie R, Nikitin AY, Hyman BT, Webb WW (2003) Live tissue intrinsic emission microscopy using multiphoton-excited native fluorescence and second harmonic generation. Proc Natl Acad Sci U S A 100(12):7075–7080. https://doi.org/10.1073/pnas.0832308100
10. Pastrana E (2012) Near-infrared probes. Nat Methods 10:36. https://doi.org/10.1038/nmeth.2294
11. Swamy A, Mason J, Lee H, Meadows F, Baars M, Strekowski L, Patonay G (2006) Near-infrared Absorption/Luminescence Measurements. In: Meyers RA, Warner IM (eds) Encyclopedia of Analytical Chemistry. https://doi.org/10.1002/9780470027318.a5410
12. Williams ATR, Winfield SA, Miller JN (1983) Relative fluorescence quantum yields using a computer-controlled luminescence spectrometer. Analyst 108(1290):1067–1071. https://doi.org/10.1039/AN9830801067
13. Jares-Erijman EA, Jovin TM (2003) FRET imaging. Nat Biotechnol 21:1387–1395. https://doi.org/10.1038/nbt896
14. Wu X, Sun X, Guo Z, Tang J, Shen Y, James TD, Tian H, Zhu W (2014) In vivo and in situ tracking Cancer chemotherapy by highly Photostable NIR fluorescent Theranostic prodrug. J Am Chem Soc 136(9):3579–3588. https://doi.org/10.1021/ja412380j
15. Lee H, Mason JC, Achilefu S (2008) Synthesis and spectral properties of near-infrared Aminophenyl-, Hydroxyphenyl-, and phenyl-substituted Heptamethine Cyanines. J Org Chem 73(2):723–725. https://doi.org/10.1021/jo701793h
16. Levitz A, Marmarchi F, Henary M (2018) Synthesis and optical properties of near-infrared meso-phenyl-substituted symmetric Heptamethine cyanine dyes. Molecules 23(2). https://doi.org/10.3390/molecules23020226
17. Matichak JD, Hales JM, Barlow S, Perry JW, Marder SR (2011) Dioxaborine- and indole-terminated Polymethines: effects of bridge substitution on absorption spectra and third-order polarizabilities. J Phys Chem A 115(11):2160–2168. https://doi.org/10.1021/jp110425r
18. Dewar MJS (1950) 478. Colour and constitution. Part I. Basic dyes. J Chem Soc (0):2329–2334. https://doi.org/10.1039/JR9500002329
19. Knott EB (1951) 227. The colour of organic compounds. Part I. A general colour rule. J Chem Soc (0):1024–1028. https://doi.org/10.1039/JR9510001024
20. Peng X, Song F, Lu E, Wang Y, Zhou W, Fan J, Gao Y (2005) Heptamethine cyanine dyes with a large stokes shift and strong fluorescence: a paradigm for excited-state intramolecular charge transfer. J Am Chem Soc 127(12):4170–4171. https://doi.org/10.1021/ja043413z
21. Gorris HH, Saleh SM, Groegel DBM, Ernst S, Reiner K, Mustroph H, Wolfbeis OS (2011) Long-wavelength absorbing and fluorescent chameleon labels for proteins, peptides, and amines. Bioconjug Chem 22(7):1433–1437. https://doi.org/10.1021/bc200192k
22. Menéndez GO, Eva Pichel M, Spagnuolo CC, Jares-Erijman EA (2013) NIR fluorescent biotinylated cyanine dye: optical properties and combination with quantum dots as a potential sensing device. Photochemical & Photobiological Sciences 12(2):236–240. https://doi.org/10.1039/C2PP25174D
23. Liu A, Wu L, He Z, Zhou J (2011) Development of highly fluorescent silica nanoparticles chemically doped with organic dye for sensitive DNA microarray detection. Anal Bioanal Chem 401(6):2003–2011. https://doi.org/10.1007/s00216-011-5258-y
24. Zhang W-H, Hu X-X, Zhang X-B (2016) Dye-doped fluorescent silica nanoparticles for live cell and in vivo bioimaging. Nanomaterials 6(81):1–17. https://doi.org/10.3390/nano6050081
25. Nooney RI, McCormack E, McDonagh C (2012) Optimization of size, morphology and colloidal stability of fluorescein dye-doped silica NPs for application in immunoassays. Anal Bioanal Chem 404(10):2807–2818. https://doi.org/10.1007/s00216-012-6224-z

26. Larson DR, Ow H, Vishwasrao HD, Heikal AA, Wiesner U, Webb WW (2008) Silica nanoparticle architecture determines radiative properties of encapsulated fluorophores. Chem Mater 20(8):2677–2684. https://doi.org/10.1021/cm7026866
27. Wang L, Yang C, Tan W (2005) Dual-Luminophore-doped silica nanoparticles for multiplexed signaling. Nano Lett 5(1):37–43. https://doi.org/10.1021/nl048417g
28. Wang L, Zhao W, O'Donoghu MB, Tan W (2007) Fluorescent nanoparticles for multiplexed Bacteria monitoring. Bioconjug Chem 18(2):297–301. https://doi.org/10.1021/bc060255n
29. Nakamura M, Shono M, Ishimura K (2007) Synthesis, characterization, and biological applications of multifluorescent silica nanoparticles. Anal Chem 79(17):6507–6514. https://doi.org/10.1021/ac070394d
30. Biffi S, Petrizza L, Rampazzo E, Voltan R, Sgarzi M, Garrovo C, Prodi L, Andolfi L, Agnoletto C, Zauli G, Secchiero P (2014) Multiple dye-doped NIR-emitting silica nanoparticles for both flow cytometry and in vivo imaging. RSC Adv 4(35):18278–18285. https://doi.org/10.1039/C4RA01535E
31. Kumar R, Roy I, Ohulchanskyy TY, Goswami LN, Bonoiu AC, Bergey EJ, Tramposch KM, Maitra A, Prasad PN (2008) Covalently dye-linked, surface-controlled, and bioconjugated organically modified silica nanoparticles as targeted probes for optical imaging. ACS Nano 2(3):449–456. https://doi.org/10.1021/nn700370b
32. Wang Z, Hong X, Zong S, Tang C, Cui Y, Zheng Q (2015) BODIPY-doped silica nanoparticles with reduced dye leakage and enhanced singlet oxygen generation. Sci Rep 5(12602). https://doi.org/10.1038/srep12602
33. Labéguerie-Egéa J, McEvoy HM, McDonagh C (2011) Synthesis, characterisation and functionalisation of luminescent silica nanoparticles. J Nanopart Res 13(12):6455–6465. https://doi.org/10.1007/s11051-011-0539-0
34. Edelstein A, Amodaj N, Hoover K, Vale R, Stuurman N (2010) Computer control of microscopes using μManager. Curr Protoc Mol Biol 92(1):14.20.11–14.20.17. https://doi.org/10.1002/0471142727.mb1420s92
35. Edelstein AD, Tsuchida MA, Amodaj N, Pinkard H, Vale RD, Stuurman N (2014) Advanced methods of microscope control using μManager software. J Biol Methods 1(2):e10. https://doi.org/10.14440/jbm.2014.36
36. Meijering EHW, Niessen WJ, Viergever MA (2001) Quantitative evaluation of convolution-based methods for medical image interpolation. Med Image Anal 5(2):111–126. https://doi.org/10.1016/S1361-8415(00)00040-2
37. Landini G Advanced shape analysis with ImageJ. In: Proceedings of the second ImageJ user and developer conference, Luxembourg, 6–7 November 2008. pp 116–121
38. Stöber W, Fink A, Bohn E (1968) Controlled growth of monodisperse silica spheres in the micron size range. J Colloid Interface Sci 26(1):62–69. https://doi.org/10.1016/0021-9797(68)90272-5
39. Nooney RI, McCahey CMN, Stranik O, Le Guevel X, McDonagh C, MacCraith BD (2009) Experimental and theoretical studies of the optimisation of fluorescence from near-infrared dye-doped silica nanoparticles. Anal Bioanal Chem 393(4):1143–1149. https://doi.org/10.1007/s00216-008-2418-9
40. Jung H-S, Moon D-S, Lee J-K (2012) Quantitative analysis and efficient surface modification of silica nanoparticles. J Nanomater 2012:8. https://doi.org/10.1155/2012/593471
41. Seminar on Adsorption BEL Japan, Inc. http://www.microtrac-bel.com/en/tech/bel/seminar06.html. Accessed 26 March 2018
42. Zielinski JM, Kettle L (2013) Physical Characterization: Surface Area and Porosity. Intertek Chemicals and Pharmaceuticals. www.intertek.com/chemical-physical-characterization-surface-area-and-porosity/. Accessed 19 August 2018
43. Murali VS, Wang R, Mikoryak CA, Pantano P, Draper R (2015) Rapid detection of polyethylene glycol sonolysis upon functionalization of carbon nanomaterials. Exp Biol Med (Maywood) 240(9):1147–1151. https://doi.org/10.1177/1535370214567615
44. Benson RA, Kues HA (1978) Fluorescence properties of indocyanine green as related to angiography. Phys Med Biol 23(1):159–163
45. Ornelas CL, Durandin A, Canary JW, Pennell R, Liebes LF, Weck M (2011) Combining Aminocyanine dyes with polyamide Dendrons: a promising strategy for imaging in the near-infrared region. Chem Eur J 17:3619–3629
46. Mchedlov-Petrossyan NO, Kukhtik VI, Bezugliy VD (2003) Dissociation, tautomerism and electroreduction of xanthene and sulfonephthalein dyes in N,N-dimethylformamide and other solvents. J Phys Org Chem 16(7):380–397. https://doi.org/10.1002/poc.654
47. Valeur B (2001) Molecular fluorescence: principles and applications. Wiley-VCH, Weinheim
48. Nyffenegger R, Quellet C, Ricka J (1993) Synthesis of fluorescent, monodisperse, colloidal silica particles. J Colloid Interface Sci 159(1):150–157. https://doi.org/10.1006/jcis.1993.1306
49. Palantavida S, Tang R, Sudlow GP, Akers WJ, Achilefu S, Sokolov I (2014) Ultrabright NIR fluorescent mesoporous silica nanoparticles. J Mater Chem B 2(20):3107–3114. https://doi.org/10.1039/C4TB00287C
50. Bhattacharyya S, Prashanthi S, Bangal PR, Patra A (2013) Photophysics and dynamics of dye-doped conjugated polymer nanoparticles by time-resolved and fluorescence correlation spectroscopy. J Phys Chem C 117(50):26750–26759. https://doi.org/10.1021/jp409570f
51. Chen X, Zhang X, Xia L-Y, Wang H-Y, Chen Z, Wu F-G (2018) One-step synthesis of Ultrasmall and Ultrabright Organosilica Nanodots with 100% photoluminescence quantum yield: long-term lysosome imaging in living, fixed, and Permeabilized cells. Nano Lett 18(2):1159–1167. https://doi.org/10.1021/acs.nanolett.7b04700
52. Soper SA, Nutter HL, Keller RA, Davis LM, Shera EB (1993) The photophysical constants of several fluorescent dyes pertaining to ultrasensitive fluorescence spectroscopy. Photochem Photobiol 57(s1):972–977. https://doi.org/10.1111/j.1751-1097.1993.tb02957.x
53. Unruh JR, Gokulrangan G, Wilson GS, Johnson CK (2005) Fluorescence properties of fluorescein, Tetramethylrhodamine and Texas red linked to a DNA aptamer. Photochem Photobiol 81(3):682–690. https://doi.org/10.1111/j.1751-1097.2005.tb00244.x
54. Martin MM, Lindqvist L (1975) The pH dependence of fluorescein fluorescence. J Lumin 10(6):381–390. https://doi.org/10.1016/0022-2313(75)90003-4
55. Klonis N, Sawyer WH (2003) The Thiourea group modulates the fluorescence emission decay of fluorescein-labeled molecules. Photochem Photobiol 77(5):502–509. https://doi.org/10.1562/0031-8655(2003)0770502TTGMTF2.0.CO2
56. Miura T, Urano Y, Tanaka K, Nagano T, Ohkubo K, Fukuzumi S (2003) Rational design principle for modulating fluorescence properties of fluorescein-based probes by Photoinduced Electron transfer. J Am Chem Soc 125(28):8666–8671. https://doi.org/10.1021/ja035282s
57. Hu Z, Tan J, Lai Z, Zheng R, Zhong J, Wang Y, Li X, Yang N, Li J, Yang W, Huang Y, Zhao Y, Lu X (2017) Aptamer combined with fluorescent silica nanoparticles for detection of hepatoma cells. Nanoscale Res Lett 12(96):96. https://doi.org/10.1186/s11671-017-1890-6
58. Jokerst JV, Lobovkina T, Zare RN, Gambhir SS (2011) Nanoparticle PEGylation for imaging and therapy. Nanomedicine 6(4):715–728. https://doi.org/10.2217/nnm.11.19

59. Wilchek M, Bayer EA (eds) (1990) Avidin-biotin technology. Methods in Enzymology, vol, vol 184. Academic Press, San Diego
60. Lesniak A, Fenaroli F, Monopoli MP, Åberg C, Dawson KA, Salvati A (2012) Effects of the presence or absence of a protein Corona on silica nanoparticle uptake and impact on cells. ACS Nano 6(7):5845–5857. https://doi.org/10.1021/nn300223w
61. Zhou G, Li L, Xing J, Cai J, Chen J, Liu P, Gu N, Ji M (2017) Layer-by-layer construction of lipid bilayer on mesoporous silica nanoparticle to improve its water suspensibility and hemocompatibility. J Sol-Gel Sci Technol 82(2):490–499. https://doi.org/10.1007/s10971-017-4330-2
62. Abdelwahab WM, Phillips E, Patonay G (2018) Preparation of fluorescently labeled silica nanoparticles using an amino acid-catalyzed seeds regrowth technique: application to latent fingerprints detection and hemocompatibility studies. J Colloid Interface Sci 512:801–811. https://doi.org/10.1016/j.jcis.2017.10.062
63. Slowing II, Wu C-W, Vivero-Escoto JL, Lin VS-Y (2009) Mesoporous silica nanoparticles for reducing hemolytic activity towards mammalian red blood cells. Small 5(1):57–62. https://doi.org/10.1002/smll.200800926
64. Lundqvist M, Sethson I, Jonsson B-H (2004) Protein adsorption onto silica nanoparticles: conformational changes depend on the Particles' curvature and the protein stability. Langmuir 20(24):10639–10647. https://doi.org/10.1021/la0484725